THE JOURNAL OF PHYSICAL CHEMISTRY B

Article

In Singulo Probing of Viral RNA Dynamics by Multi-chromophore Fluorescence Dequenching

Virginia Smith, and Bogdan Dragnea

J. Phys. Chem. B, **Just Accepted Manuscript** • DOI: 10.1021/jp510853r • Publication Date (Web): 12 Nov 2014

In Singulo Probing of Viral RNA Dynamics by Multi-chromophore Fluorescence Dequenching

Virginia M. Smith[†] and Bogdan Dragnea[*,‡]

Department of Molecular and Cellular Biochemistry, Indiana University, Bloomington, IN 47405, USA, and Department of Chemistry, Indiana University, Bloomington, IN 47405, USA

E-mail: dragnea@indiana.edu

[*]To whom correspondence should be addressed
[†]Department of Molecular and Cellular Biochemistry, Indiana University, Bloomington, IN 47405, USA
[‡]Department of Chemistry, Indiana University, Bloomington, IN 47405, USA

Abstract

Current understanding of virus life-cycle states and transitions between them is mainly built on knowledge of the protein shell structure encapsulating the genome. Little is known about the genome fate during viral transitions. Here, changes in the fluorescence rate from multi-labeled transcript viral RNAs encapsulated in Brome mosaic virus capsids were examined as a function of the RNA state. A simple kinetic model relating chain compactness to single-molecule fluorescence emission suggests that in a dense multichromophore system, the rate of energy transfer should scale with distance more gradually than the rate of the Förster energy transfer between two chromophores, which varies sharply as the reciprocal of distance to the sixth power. As a proof-of-principle experiment, we have compared predictions from a numerical model for confined diffusive motion with the fluorescence emission from virus-encapsulated, and free single RNA molecules decorated with multiple cyanine dyes and encapsulated inside microscopic emulsion droplets. We found that the effective quantum yield per labeled particle depends on the expansion state in agreement with theoretical predictions. Since fluorescence single particle tracking is now a well-established methodology for the study of virus-life cyle, the findings reported here may pave the way towards reducing the existing gap between *in vitro* and cellular *in singulo* studies of the fates of viral RNA.

Keywords

single virus dynamics, viral RNA release, fluorescence

Introduction

Chain compactness is a central concept in considerations regarding the structure-function relationship in proteins and nucleic acids. Thus, protein chain compactness, the result of hydrophophic collapse, is a key factor in secondary structure stabilization.[1] For large RNA

molecules such as the single stranded RNA of viral genomes, chain compactness contributes to the ability of the virus to assemble efficiently.[2] Therefore, measuring chain compactness in real-time could lead to a better understanding of the fundamentals of broadly important phenomena such as protein folding and virus-host interactions. For instance, the ability of measuring fluctuations in the compactness of a RNA molecule could provide valuable supplemental constraints for computations or validations of theoretical tertiary structure predictions.[3] Nevertheless, current methods for measuring chain compactness have limitations due to the fact that they deal with bulk averaging such as time-resolved small angle X-ray scattering (SAXS) or because they are restricted to *ex-vivo* applications, such as cryo-electron microscopy.

Optical microscopy methods are time-resolved and live cell compatible. One of the most wide-spread optical methods for the measurement of real-time conformational changes is the Förster resonant energy transfer (FRET) single-molecule spectroscopy.[4] In single-molecule FRET, the sharp distance dependence of energy transfer between two chromophores with overlapping emission and absorption spectral bands is used to measure changes in the distance between the locations of the fluorescent tags as a function of time, chemical environment, etc.[5] However, the short range over which FRET is sensitive to changes in the distance between the donor and acceptor also limits the spatial scale over which structural transformations can be followed. Here we consider the problem of a spatially-extended, global quaternary structure transformation known to occur a few small icosahedral plant viruses. Such a transformation would be hard, in principle, to follow using two-chromophore FRET, but the results presented in this article suggest that a scale extension is possible in the case of multiple homo-FRET. The quaternary structure transformation we are dealing with is a redistribution of the coat protein in the virus shell in a less compact lattice, triggered by a chemical cue. The result is an overall swelling of the shell, and possibly a redistribution of the virus genome. Due to the absence of *in vivo* measurement methods, its biological significance has not yet been firmly established. However, it has been suggested that the dramatic

reorganization of the coat proteins has to do with RNA presentation prior to replication. Little is currently known about the fate of viral RNA during virus coat reorganization.

In this article, an optical microscopy approach is described which is able of following changes in RNA chain compactness in real time, as the virus capsid undergoes a swelling transition. The method relies on densely labeling viral RNA with identical, coupled chromophores, and measuring fluorescence emission as a function of time. As a proof-of-principle experiment, changes in RNA compactness were obtained by single particle total internal reflection fluorescence (TIRF) microscopy during the pH-induced swelling of a virus-like particle (VLP) derived from the Brome mosaic virus (BMV). It was found that the transition occurs in less than 2 seconds, which is the limit set by buffer exchange rate. The magnitude of fluorescence intensity change is large enough to warrant explorations of extending the method to living cell studies. Moreover, it was found that for a multiple-labeled macromolecular chain, the spatial dynamic range over which a structural transformation can be followed significantly exceeds that achievable by conventional two-chromophore FRET. A simple model relating the fluorescence quantum yield to chain compactness was employed to estimate the degree of RNA molecule confinement in different states.

Multiple labeling of viruses and virus capsids has been previously employed in a variety of investigations, for instance in applications to light harvesting arrays,[6] the loading of fluorescent polymers and small organic dyes in virus-like particles by self-assembly,[7,8] for quantifying the loading capacity of phage capsid containers,[9] and for single particle tracking in cells.[10] More closely related to the emphasis on chromophore coupling in this work, Luchowski et al. studied the fluorescence emission from multiple fluorophores immobilized on a single antibody and identified specific benefits of over-labeling for single-molecule experiments such as the number of available photons and the increase in the overall survival time.[11] Fluorescence life-time was discussed as a probe for internal dynamics of macromolecules multi-labeled with excimer-forming dyes[12] and fluorescence correlation spectroscopy assays have been employed to monitor the conformations of viral genomes and sub-fragments with and without

coat proteins.[13] Site-directed spin labeling was employed to monitor transitions in a protein cage over spatial ranges typical for electron paramagnetic resonance spectroscopy.[14] However, to the best of our knowledge, there were no attempts to experimentally determine the dependence of quantum yield on the degree of chain compactness or to model steady state fluorescence emission from densely labeled, dynamic macromolecule undergoing expansion or compression.

BMV is a non-enveloped plant virus formed of an icosahedral, 28 nm shell made of 20 hexamers and 12 pentamers of the same protein encapsulating 1-2 positive sense RNA molecules. Its entire genome is constituted of 4 RNA molecules partitioned inside three morphologically indistinguishable particles.[15,16] BMV was widely used as a model system for a class of small icosahedral plant viruses sharing a global, reversible transition in the quaternary structure of their coat. This transformation, which is observable *in vitro* when the pH of the medium changes from acidic to neutral in presence of chelators, is accompanied by an increase of $\sim 11\%$ in diameter.[17,18] Since the swelling transition is believed to play a role in the viral RNA presentation or release by the virion,[19,20] RNA chain compactness is expected to change upon capsid swelling. However, there has been no direct confirmation of this hypothesis from experiments performed *in vitro* or in cells. It is worth noting that this example is an illustration of a broader fact about physical experiments on viruses: methods that could provide direct comparisons of virus dynamics in cells and *in vitro* assays are lacking. While the investigations discussed here have been performed *in vitro*, the approach shows promise to be applicable *in vivo*, as well.

Experimental

VLP preparation

Fluorescent labeling of RNA

Transcript RNAs were labeled with a MirusBio Label IT reagent containing Cy5 connected to a linker that facilitates electrostatic interactions, attached to a reactive alkylating group that covalently attaches to RNA. This covalent linkage is important to prevent random attachment to other charged molecules. The labeled RNA was purified from free unlabeled dyes by ethanol precipitation and resuspended in RNAse-free water. The major alkylation site is the N7 position of guanine. However other bases are also alkylated to a lesser degree including N1 and N3 of adenine (A), N3 of cytosine (C) and O6 of guanine base (G). According to MirusBio, labeling efficiencies of one label every 20-60 nucleotides of ssRNA is achieved with higher efficiency labeling to guanine. The labeling density was controlled by varying the incubation time at a set temperature of 37°C.

Gel electrophoresis of nondenatured and glyoxal-denatured labeled RNA was run on 0.8% agarose gel in BPTE buffer with unlabeled transcript RNA as the marker. RNA was denatured by incubation in glyoxal at 55°C for 30-60 minutes followed by a 10 minute incubation on ice. This method is used to assure that dye binding did not perturb the normal migration of RNA on the gel. Agarose gels were imaged using the Typhoon Variable Mode Imager (Amersham Biosciences).

The density of labels on RNA was determined by UV-Vis absorption spectrometry and fitting the spectrum of dye-labeled RNA by multilinear regression with two extinction spectra from pure Cy5 and pure RNA.

RNA transcription

BMV RNA was synthesized by *in vitro* transcription using the T7 system (plasmid pB2TP5 was provided by Dr. Cheng Kao, Indiana University). The plasmid contains full-length

cDNA clones corresponding to BMV RNA2 (2.8kb). The plasmids were linearized with EcoRI, purified by Qiagen miniprep kit and run on a 1.2% agarose gel in 1X TAE (Tris-acetate-EDTA) buffer to verify full excised plasmid. The linearized plasmid was then transcribed with the AmpliCap-Max T7 RNA transcription kit by Epicentre Biotechnologies. The RNA was verified by gel electrophoresis on a 0.8% agarose gel in 1X BPTE (300mM Bis-Tris, 100mM PIPES, and 10 mM EDTA) buffer with extracted native BMV RNAs as a marker.

Purification of BMV capsid protein

FPLC purified BMV capsids were disassembled by dialysis in disassembly buffer (0.5M $CaCl_2$, 0.05M Tris, pH 7.5) at 4°C overnight and RNA precipitant was removed by ultracentrifugation at 40K rpm for 1 hour at 4°C in a Beckman TLA110 rotor. The supernatant was then extracted and dialyzed against Tris buffer (0.01M Tris, pH 7.4) for 24 hours at 4°C. The protein was then stabilized in protein buffer (0.02M Tris, pH 7.4, 1.0M KCl, 0.005M $MgCl_2$) by dialysis at 4°C for 24 hours. The concentration and purity were confirmed by UV spectrophotometry at a 260/280 ratio between 0.60-0.62.

Virus-like particle reassembly and purification

Assembly of purified capsid protein and labeled RNA was achieved by dialysis of a mixture against virus reassembly buffer (0.05M Tris, pH 7.2, 0.05M NaCl, 0.01M KCl, 0.005M $MgCl_2$) for at least 24 hours at 4°C followed by dialysis in virus buffer (SAMA: 0.05M NaOAc, pH 4.6, 0.008M Mg$(OAc)_2$) for an additional 24 hours at 4C. The assembly mixture contained capsid proteins and RNA in a 3:1 ratio. To confirm assembly, 10 μl of each assembly mixture in SAMA were incubated on carbon coated 300 mesh copper grids, stained with 1% uranyl acetate and imaged using 60,000x magnification on the JEOL 1010 transmission electron microscope (Electron Microscopy Center, Indiana University). The VLPs were purified by a 10% sucrose cushion to pellet VLPs using a Beckman TLA110 rotor at

30K RPM for 45 minutes. The VLPs were then resuspended and dialyzed in SAMA buffer for about 48 hours at 4°C to remove sucrose. The VLPs were then concentrated using 100K Amicon Ultra Centrifugal Filters and stored at 4°C.

Methods

Microscopy

An inverted Nikon Ti microscope fitted with a TIRF assembly (Nikon) and a Revolution XD laser control system (Andor Technology, South Windsor, CT) was used for single-molecule imaging. Samples were excited through a high-numerical aperture 100x oil-immersion objective (CFI APO TIRF, NA 1.49, Nikon) with a 640 nm laser (40 mW before the TIRF assembly). Fluorescence was collected back through the objective, passed through a band-pass emission filter (685/40, Semrock) to eliminate residual laser light, and recorded on an EM-CCD camera iXon DU-897-BV (Andor Technology). Andor iQ software was used for image acquisition. Imaging frame rate was 20 Hz. At least 1000 frames were collected for every imaged region. At least 10 regions were imaged and analyzed for every sample.

Images were processed and analyzed using ImageJ (National Institutes of Health, Bethesda, MD) and IgorPro (Wavemetrics) software. For RNA and VLPs samples a square ROI (7x7 pixels) was used to obtain integrated intensity collected from a single particle. The average integrated intensity from the first 5 frames was used to generate histograms of intensities.

To increase the likelihood for an individual spot on the CCD frame to correspond to a single RNA or a single VLP, only diffraction-limited spots were included in the analysis, and only if their time-averaged initial intensity was within the confidence limits provided by the statistical analysis of intensity histograms as a function of concentration.

For emulsion work, the stack of 200 first frames was summed to obtain an averaged image of droplets. A circular region of interest with diameter 17 pixels (area is 225 pixels) was used to choose droplets with diameter less than 3 μm. Droplets of diffuse interior corresponded to those encapsulating RNAs in Brownian motion. Diffuse droplets with diameters less than

the ROI were picked up for analysis. For every droplet, a background ROI with the same diameter was chosen from nearest proximity and subtracted from the signal.

Coverslip preparation

Glass coverslips were cleaned by piranha (3:1 H_2O_2:H_2SO_4)treatment for 1 hour and washed for 5 minutes with double-distilled miliQ water. Clean coverslips were stored in water and dried by burning with a propane torch before use.

For the emulsion assay, piranha-cleaned coverslips were treated with octadecyltrimethoxysilane to obtain a hydrophobic surface. Silanisation was performed by immersing dried coverslips in 1% silane solution in hexane for 30 minutes, then rinsed one time with hexane and two times with methanol and incubated overnight at 60°C to dry.

pH-Induced VLP swelling

A clean, non-functionalized coverslip pressed against a Grace Biolabs coverwell perfusion chamber (3-3mm X 32mm X 0.6mm depth, 26 X 43 mm, OD/ 1.5mm diameter ports) was used to exchange buffer conditions in order to initiate pH-induced changes of VLPs. After a 5-minute incubation of VLPs in SAMA buffer (0.05M NaOAc, 0.008M Mg(OAc)2, pH 4.6) on the coverslip, VLPs were imaged for about 3 secs in SAMA before exchange with 200 mM EDTA (pH 6.0). The buffer was exchanged by adding 60 μl of the new buffer to one port and simultaneously absorbing old buffer through the other port. Re-focus accuracy after mixing is better than 50 nm (per manufacturer technical notes) and therefore intensity changes due to a re-focus artifact after mixing are negligible. However, to further avoid possible artifacts related to defocus and sample shift, for time resolved studies, we have used spot-integrated intensities from a matrix of pixels around the spot center.

Emulsion droplet preparation and measurement

100 μl of 1nM RNA solution was mixed with $C_{12}E_8$ surfactant at 0.5-1% by volume. 10μl of this mixture was added to 200 μl of FC770 and ultrasonicated (Branson 5510) for 10-15 seconds at room temperature. Immediately after sonication, 60 μl of the obtained emulsion was added to the channel made of functionalized coverslip and perfusion chamber gasket.

The emulsion formed from a mixture of 100 nM fluorescein solution and 100 nm carboxylated fluorescent beads was used for initial droplet characterization. Confocal microscopy was employed to image droplets at 0.25 μm interval in a direction normal to the coverslip surface. RNA concentrations were kept low to ensure that a droplet contains either no or one RNA molecule at most. The diameter and thickness of emulsion droplets was measured post-aquisition with ImageJ software. Majority of the sample contained droplets with diameters less than 5 μm and thickness less than 500 nm. Three different surfactants: $C_{12}E_8$, SDS, and Tween 20 were tested to reduce potential droplet surface/RNA interaction. In the case of $C_{12}E_8$ the majority of droplets contained diffusing beads and very few beads were stuck at the droplet interface. The $C_{12}E_8$ surfactant was thus selected for further work.

Results and discussion

Results from time-lapse fluorescence intensity measurements are introduced first. In these experiments, single VLPs were adsorbed on a silica coverslip at pH 4.6. Each VLP contained one BMV RNA2 molecule labeled with $\sim$N = 26 Cy-5 chromophores in average. After $\sim$ 2 s from the start of the CCD time-lapse recording, the buffer was exchanged with the EDTA (pH 6.0) buffer. Fig. 1 shows a sequence of frames, at 2 s/frame, illustrating the changes in intensity observed during the buffer exchange process. Spot-integrated intensities from 4 particles are presented as a function of time at 50 ms/step, in Fig. 2. All traces start off at an initial intensity of $\sim 1.0 \times 10^3$ – 2.0×10^3 cts/s. Immediately after the buffer it replaced and the sample equilibrated, the particles become brighter (maximum intensity levels rising

to $\sim 6.0 \times 10^3 - 8.0 \times 10^3$ cts/s). Sample equilibration is defined here as the moment in time when the interferometric focus feedback loop was restored.

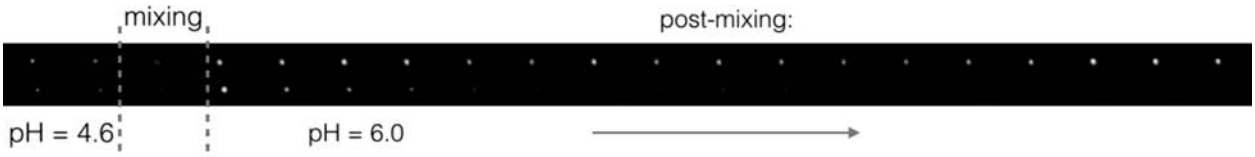

Figure 1: A montage of TIRF frames at 2 s per frame for two representative particles illustrating the main states along the experimental procedure: pre-mixing, transient defocusing due to mixing and equilibration, post-mixing. There is clear post-mixing intensity increase.

The exact moment at which maximum intensity is reached seems to occur either before equilibration (top traces in Fig. 2) or quickly after (bottom traces in Fig. 2). The magnitude of the last step allows for an estimation of emitted intensity per unperturbed individual chromophore. A comparison of sample-averaged bleaching decays before and after the pH jump suggests that fluorescence from VLPs bleaches approximately twice as fast at pH 6.0 than at pH 4.6, Fig. 3. Control fluorimetry experiments of free Cy5 dyes in solutions of different pH indicated that free Cy5 fluorescence intensity is lower at pH 6.0 than at pH 4.6. Therefore, the observed fluorescence increase for VLPs upon an increase in pH cannot be simply the result of free dye behavior. Moreover, bleaching decays of free Cy5 in solution were largely unaffected by pH. We conclude that the jumps observed in VLP fluorescence intensity and bleaching time cannot be attributed to the properties of free Cy5 and have to do with changes in the dye environment, i.e. in the viral RNA state.

To account for the fluorescence baseline decay and obtain more accurate information about the magnitude and dynamics of the observed fluorescence intensity jump, we have normalized the average of 20 VLP fluorescence time-course traces by the fluorescence decay curve of VLPs at pH 4.6, Fig. 4. The normalized average fluorescence trace starts and ends at a relative intensity of 1.0. A maximum relative intensity of 20 is reached in 1.6 s (value obtained from a sigmoidal fit of the fluorescence increase), after which the intensity decreases mono-exponentially. The 1.6 s duration of the upward ramp was comparable with the speed at which the pH changes (data not shown). Therefore, the characteristic time for

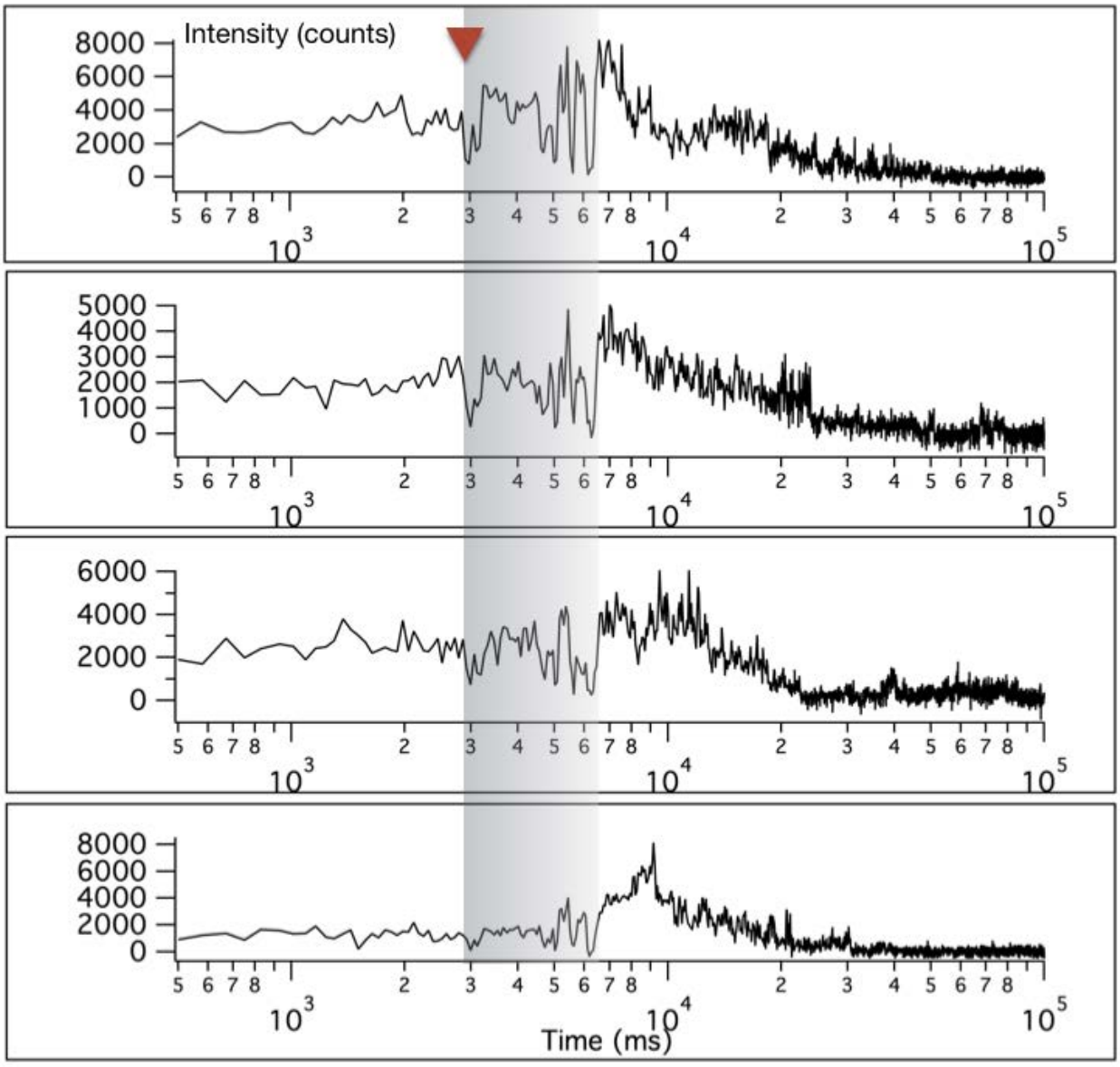

Figure 2: Typical time course fluorescence emission from single VLPs undergoing a swelling transition triggered by pH increase. The shaded area approximately represents the span of mixing and equilibration processes. The arrow indicates the start of buffer exchange. The end of the shaded area corresponds to the PSF control bringing the sample back in focus.

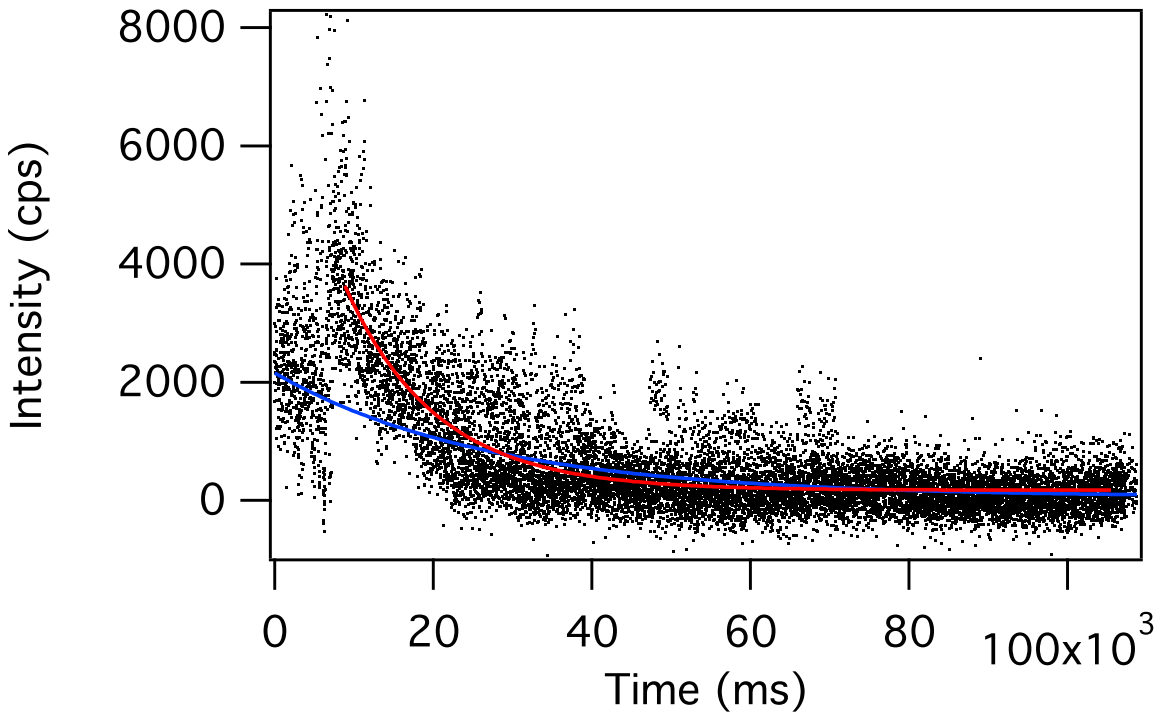

Figure 3: Fluorescence emission vs. time (dots) from 20 particles undergoing a pH jump. The pH jump had a duration of 2 s and a start point at t = 6 s. Red line: exponential decay fit for data after pH jump. Blue line: exponential decay fit of data collected at pH 4.6 (data not shown).

the pH-induced transition of VLPs must be less than 1.6 s, if indeed fluorescence intensity changes are due to a change in the chromophore environment due to the VLP transition.

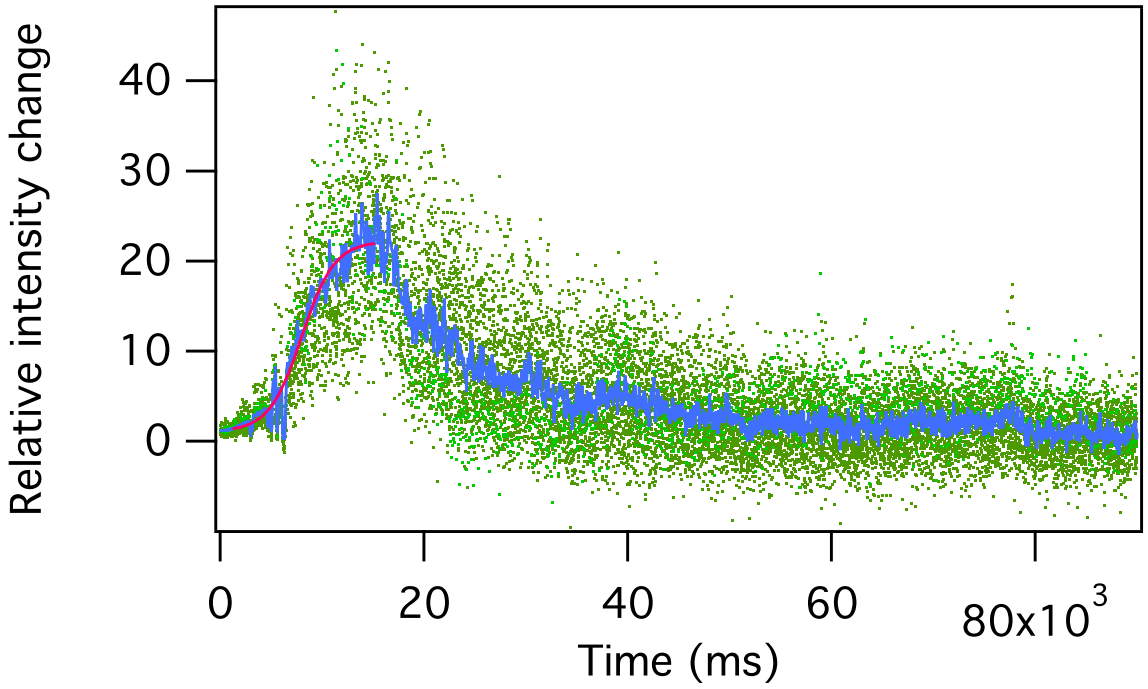

Figure 4: Normalized fluorescence change from 20 VLPs undergoing a pH jump relative to fluorescence at pH 4.6 (green dots). Red line: sigmoidal fit of the average trace (blue).

To examine this hypothesis we have measured the fluorescence emission from viral RNAs decorated with Cy5 at three equilibrium states, corresponding to three pH values: pH 4.5, pH 6.0, and pH 7.0, and from labeled single RNA molecules entrapped in detergent stabilized emulsion droplets of $\sim$ 0.5 - 2.0 μm diameter, at pH 7.0. In the later state, the RNA is expected to be fully expanded, while VLP states corresponding to the RNA being complexed with CP correspond to morphologies of presumably varying compactness, Fig. 5.

In these experiments, the fluorescence intensity from single VLPs was first measured as a function of time. Photobleaching caused intensity vs. time traces to decay in roughly exponential fashion terminated by a sudden step (see Supporting Information, Figure SI-1). Total average intensities emitted by one particle during the first 5 frames were then normalized to the intensity of this last bleaching step in the experimental traces, and then

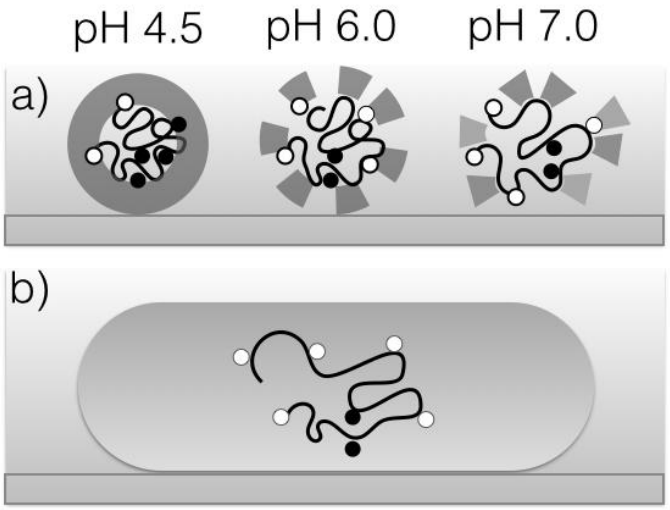

Figure 5: Equilibrium experiment schematic: (a) labeled RNA encapsulated inside VLPs in buffer at different pH values. (b) labeled RNA in droplet adsorbed from emulsion on the coverslip surface. White dots: active chromophores, black dots: quenched chromophores

divided by the average number of chromophores. The result is a relative quantum yield, Q_f, which describes the efficiency of fluorescence emission from a single RNA molecule decorated with N chromophores, relative to the emission from N non-interacting chromophores. The experimental Q_f was calculated from data with the formula:

$$Q_f \approx \frac{I_0}{I_{step} * N} \tag{1}$$

Where I_0 represents the initial intensity value, and I_{step} is the average magnitude of the last bleaching step. Note that Q_f is insensitive to the actual local field intensity (unknown).

Q_f histograms were generated from $\sim$ 100 VLPs and from droplets containing single RNA molecules. The results are presented in the form of a box-and-whisker plot, Fig.6 (see Supporting Information, Figure SI-2, for histograms of Q_f corresponding to results in Fig. 6).

Changes in the radius of gyration of the VLP complex in the conditions of Fig. 6 were measured by dynamic light scattering (DLS), (Supporting information, Figure SI-3). The radius of gyration increased from 14 nm to 22 nm upon a pH shift from pH 4.5 to pH 7.0,

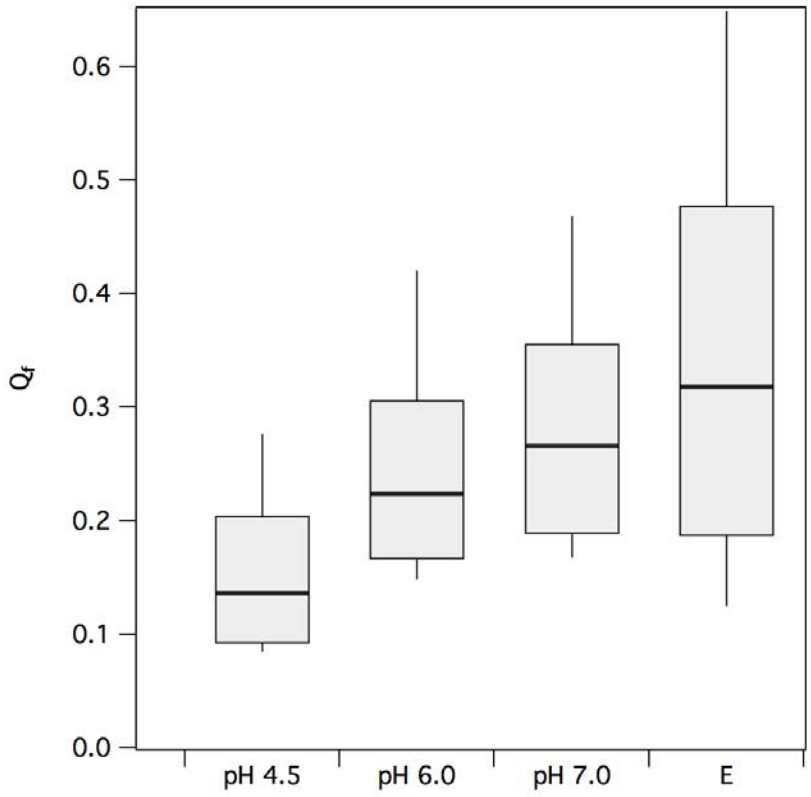

Figure 6: Box-and-whisker plot of Q_f for RNA encapsulated in VLPs at different pH values (pH 4.5 to 7.0) and for RNA inside a microscopic emulsion droplet (E).

and chelator addition. These DLS estimates compared well with previous knowledge from cryo-em structural studies.[18] Average fluorescence intensity increased with increasing pH. Intensities from free RNA inside droplets were greater in average than those from any VLP state. Data was not corrected for the pH influence on the chromophore quantum yield, which has the opposite trend with pH and thus cannot be responsible for the observed increase in average intensity with pH. Intensity fluctuations from particle to particle also increased with pH. These fluctuations are much larger than the measurement shot noise and extend asymmetrically towards the higher intensities end, Fig. 6. This suggests that there is an increase in the number of different fluorescence states as the capsid expands (at neutral pH) or when the RNA is free in solution.

These results point to a relationship between RNA fluorescence and capsid expansion. In the following, we provide a simple model that reproduces the most salient features of experimental data and provides a way to semi-empirical data interpretation by calibration against known end states.

Consider a long macromolecule decorated by N identical chromophores. At steady state, the number of excited chromophores, N*, depends on the rates of de-excitation by radiative or non-radiative transfer, k_r and k_n, respectively:

$$N^* = \frac{C}{k_r + k_n} \tag{2}$$

with C being a constant proportional to the absorbed power.

The number of photons emitted per unit time is:

$$N^* \cdot k_r = \frac{C \cdot k_r}{k_r + k_n} \tag{3}$$

The maximum radiative rate for one RNA molecule containing N chromophores is:

$$k_r(N) = N \cdot k_0 \tag{4}$$

where k_0 is the radiative rate constant for a single unperturbed chromophore. The non-radiative energy transfer rate between two chromophores free to rotate and located at the distance R from each other is given by:[5,21]

$$k_n = \frac{1}{\tau_0}\left(\frac{R_0}{R}\right)^6 \tag{5}$$

where R_0 is the isotropic Förster radius, and τ_0 is the unperturbed fluorescence lifetime. We will be assuming in the following that this is the dominating process that affects fluorescence quantum yield within the spectral bandwidth of our detection. Note that the validity of the argument behind the feature of an expanded spatial dynamic range will persist no matter the exact mechanism for quenching, provided it depends on the distance between chromophores. In a system of N chromophores, the total non-radiative energy transfer rate will be given by:

$$k_n(N) = \frac{R_0^6}{\tau_0} \cdot \sum_{j=1}^{N-1} \sum_{i=j+1}^{N} \frac{1}{R_{ij}^6} \tag{6}$$

with R_{ij} being the distance between chromophore i and chromophore j.

In these conditions, the quantum yield Φ_N for an RNA molecule containing N chromophores, which is defined as the rate of fluorescent emission over the rate of absorption reads:

$$\Phi_N = \Phi_0 \cdot \frac{1}{1 + \tau_0 \cdot k_n(N)} \tag{7}$$

where Φ_0 represents the quantum yield of an unperturbed system of N chromophores that are separated by large distances from each other.

To allow for a comparison between theoretical predictions and experimental data, it is convenient to use relative quantum yield as a measure of non-radiative coupling independent of excitation laser parameters:

$$Q_f = \frac{\Phi(N)}{\Phi_0(N)} \tag{8}$$

Q_f is a random variable since for a flexible molecule the R_{ij} values and subsequently the pairwise transfer rates are expected to fluctuate considerably as a function of time. To find its distribution function, a Brownian dynamics simulation of chromophore locations based on the freely jointed chain model[22] confined to the interior of a sphere of radius R_g was used. This simple model ensures that the length of the RNA molecule remains constant during random fluctuations. The model does not provide realistic detail on the time-dependent fluctuations but those are not important for the measurable average quantities with which we are concerned here (average self-quenching range, intensity distribution, and trends in bleaching rate as a function of confinement).

Typical calculated relative quantum yield Q_f fluctuations as a function of time are shown in Fig. 7 (a-e). Data are from a model with 20 chromophores confined to a spherical volume which expands from 9 nm to 40 nm radius. Q_f fluctuates in time as a result of inter-chromophore distance variations during the course of Brownian motion. Q_f histograms in Fig. 7 (f-j) correspond to the time traces for each R_g (a-e), respectively. There is a clear qualitative change in response to expansion. However, the most intriguing feature is the spatial range over which fluorescence changes are still sensitive to expansion. This spatial range greatly exceeds that of the typical two chromophore FRET range of ~ 6 nm. A second finding is that the qualitative histogram dependence on confinement or chain compactness potentially provides a principle for identification of the different stages of a hypothetical expansion. Thus, a histogram that is peaked close to $Q_f = 0$ will indicate a dominant non-radiative transfer rate associated with a compact state, while a peak closer to $Q_f = 1$ would indicate an expanded state from the point of view of self-quenching. In other words, if a multiple-labeled macromolecule were undergoing an expansion, its fluorescence intensity distribution would be expected to evolve similar to changes observed from (f) to (j) in Fig. 7.

Turning our attention to the apparent extended spatial range for multiple homo-FRET, we can identify two possible reasons for it. The first relates to Brownian dynamics. A flexible

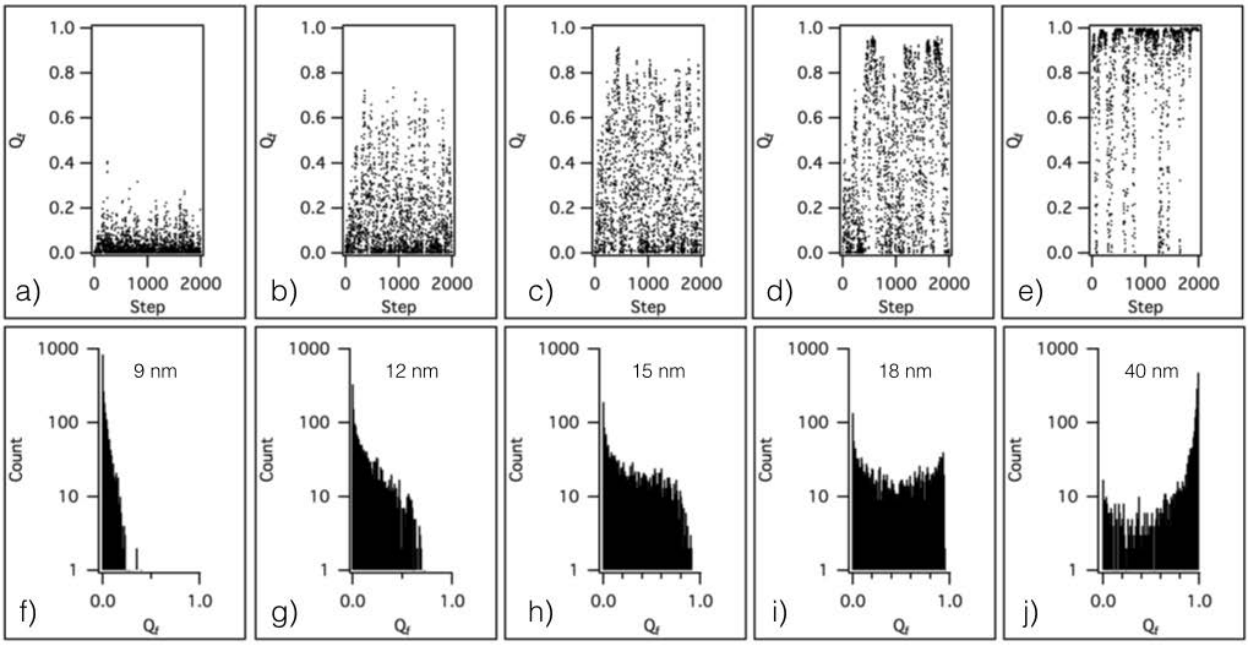

Figure 7: (a-e) Calculated time-course relative quantum yield for 20 chromophores randomly linked to a freely-jointed RNA chain model which is confined to a spherical space of 9, 12, 15, 18, and 40 nm radii respectively. (f-j) Histograms of the effective quantum yield corresponding to the time-course traces in (a-e).

molecule will explore in time conformations corresponding to high or low quenching. These different conformations manifest as dim or bright states with relative weights and result in a detection of time-averaged emission intensity that depends on the degree of confinement. The second effect comes from the energy transfer rate being a summation over all distances separating it from potential acceptors, which effectively increases the interaction length (eq. (5)). A familiar similar situation occurs, for instance, in the case of the Coulomb field which varies with distance as $1/R^2$ for an individual charge, while for a planar charge distribution, the field is independent of distance on account of integration over the entire charge distribution.[23]

As a consequence, the average $< Q_f >$ value is expected to change from 0 to 1 as the radius of the confinement volume increases. A systematic study of the $< Q_f >$ dependence on radius is presented in Figure 8. As suggested by the analysis of the data in Figure 7, the average Q_f gradually increases with the expansion of the cavity confining the chromophore

system. The slope of the Q_f increase resulting from expansion depends on the number of chromophores attached to the macromolecule. The larger the number of chromophores, the more gradual the Q_f increase upon radial expansion. As a consequence, sensitivity to expansion but limited range will characterize a small set of chromophores, while maximum range will be achieved for the largest number of chromophores. The spatial dynamic range for 20 chromophores is predicted in our model to span an impressive range, from $\sim$ 5 to 80 nm, Figure 8.

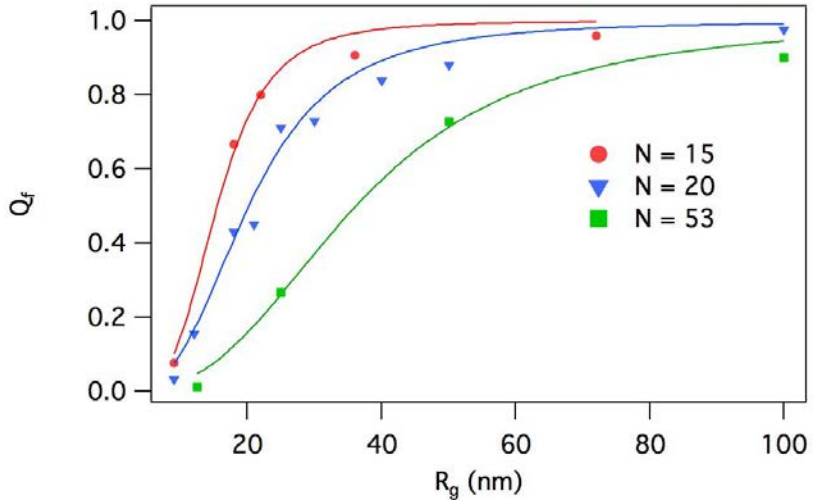

Figure 8: Effective quantum yield as a function of R_g the radius of the sphere to which the flexible macromolecule is confined. Symbols: data from Brownian dynamics simulation. Lines: Fit using relation (9). Fit parameter ϵ provided in Table 1.

Guided by the idea of an extended effective interaction range by integration over a spatially-distributed ensemble, we have attempted to fit the data (markers) in Figure 8 with a power-law expression, which results in the correct homo-FRET expression for Q_f if N = 2:

$$Q_f = \frac{1}{1 + a/R_g^{\epsilon}} \tag{9}$$

where a is a constant and ϵ is the exponent (fit parameter) which characterizes the effective range of interaction. The exponent in this phenomenological formula is a measure

of the effective spatial dynamic range. Table 1 summarizes the observed dependence of this range parameter, ϵ on the number of chromophores, N.

Table 1: Fit values for the power-law exponent parameter depend on the number of chromophores

N	2	15	20	53
ϵ	6.0	4.0	3.0	2.8

The simulation results in Fig. 8 can be directly compared with the experimental data in Fig. 6 for a semi-quantitative evaluation of changes in RNA compactness consequent to the pH-induced swelling. It is assumed that the RNA became less compact as the pH increased, and was the least compact when the viral coat protein was not present at all (in emulsion droplets). By using expression (9) with N = 25, it was found that for VLPs the average RNA radius of gyration was ∼10 nm at pH 4.5, (∼19 nm) at pH 7.0. The latter value suggests that the average space occupied by the RNA at pH 7.0 is greater than the VLP size. This could be the case since, as the pH increases, the strength of attractive interaction between protein subunits progressively weakens[24] and the capsid is believed to become increasingly disordered until eventually forms a nucleoprotein complex of a greater average radius of gyration than the swollen virus.[25] Remarkably, for free RNA in emulsion droplets the average radius of gyration is not much greater: ∼25 nm. RNA molecules are not much more extended in absence of protein than in presence of protein. This consistent with previous findings of a pre-compressed viral genome for a similar plant virus.[26,27] However, since for unlabeled viral RNA pre-compression is believed to be the result of RNA secondary structure, it is unclear how much the dye might have perturbed the RNA secondary structure and thus compactness, in the current study.

A less compact state for encapsulated RNA at higher pH is also expected to lead to increased time spent by the chromophore in the excited state since the non-radiative rate is lower in this case. Longer time periods in the excited may lead to bleaching. The observation

of increased bleaching (Fig. 3) upon swelling can be explained this way. Another effect that may contribute to bleaching is the enhanced access of chromophores to reactive oxygen species in solution due to opening of pores in the capsid during swelling. Furthermore, expansion of the volume available to RNA would also increase sampling of different states and thus of fluctuations in the relative quantum yield, a feature that can be observed in qualitatively corroborating manner in Fig.6 and Fig. 7.

In conclusion, we have investigated the use of multi-chromophore labeling of a viral RNA molecule with the purpose of non-intrusively evaluating RNA chain compactness at different stages of confinement. We have found that the rate of homo-FRET in a multichromophore system depends on the spatial scale of confinement. The spatial dynamic range of multi-chromophore FRET was found to significantly exceed that of two-chromophore FRET. This aspect effectively increases the spatial range over which one could track morphological changes in macromolecular complexes. An application which could benefit from this idea is the release of viral RNA upon entry and disassembly inside a cell. *In vitro* real-time experiments on single BMV-like particles suggest that conventional fluorescence microsopy with single particle tracking could be employed to detect differences in viral RNA compactness over a range of conditions which affect RNA confinement, including those encountered in cells.

Acknowledgement

This work was supported by the U.S. Department of Energy, Office of Science, Basic Energy Sciences, under Award DE-SC0010507. Dr. Irina Tsvetkova's help with single-particle optical microscopy is gratefully acknowledged. The authors thank Dr. Cheng Kao for helpful discussions and for access to biochemical instrumentation in his lab.

Supporting Information Available

Characterization data including single particle fluorescence, histograms of average intensities, and dynamic light scattering results.

This material is available free of charge via the Internet at `http://pubs.acs.org/`.

References

(1) Dill, K. A.; MacCallum, J. L. The Protein-folding Problem, 50 Years On. *Science* **2012**, *338*, 1042–1046.

(2) Yoffe, A. M.; Prinsen, P.; Gopal, A.; Knobler, C. M.; Gelbart, W. M.; Ben-Shaul, A. Predicting the Sizes of Large RNA Molecules. *Proc. Natl. Acad. Sci. U. S. A.* **2008**, *105*, 16153–16158.

(3) Hajdin, C. E.; Ding, F.; Dokholyan, N. V.; Weeks, K. M. On the Significance of an RNA Tertiary Structure Prediction. *RNA-A Publ. Rna Soc.* **2010**, *16*, 1340–1349.

(4) Lakowicz, J. R. *Springer*; Springer, 2006.

(5) Valeur, B.; Berberan-Santos, M. N. *John Wiley Sons*, 2nd ed.; John Wiley & Sons: New York, 2013.

(6) Miller, R. A.; Stephanopoulos, N.; McFarland, J. M.; Rosko, A. S.; Geissler, P. L.; Francis, M. B. Impact of Assembly State on the Defect Tolerance of TMV-based Light Harvesting Arrays. *J. Am. Chem. Soc.* **2010**, *132*, 6068–6074.

(7) Cadena-Nava, R. D.; Hu, Y.; Garmann, R. F.; Ng, B.; Zelikin, A. N.; Knobler, C. M.; Gelbart, W. M. Exploiting Fluorescent Polymers to Probe the Self-assembly of Virus-like Particles. *J. Phys. Chem. B* **2011**, *115*, 2386–2391.

(8) Da Poian, A. T.; Gomes, A. M.; Coelho-Sampaio, T. Kinetics of Intracellular Viral

Disassembly and Processing Probed by Bodipy Fluorescence Dequenching. *J. Virol. Methods* **1998**, *70*, 45–58.

(9) Lucon, J.; Qazi, S.; Uchida, M.; Bedwell, G. J.; LaFrance, B.; Prevelige, P. E.; Douglas, T. Use of the Interior Cavity of the P22 Capsid for Site-specific Initiation of Atom-transfer Radical Polymerization with High-density Cargo Loading. *Nat. Chem.* **2012**, *4*, 781–788.

(10) Whitt, M. A.; Mire, C. E. Utilization of Fluorescently-labeled Tetracysteine-tagged Proteins to Study Virus Entry by Live Cell Microscopy. *Methods* **2011**, *55*, 127–136.

(11) Luchowski, R.; Matveeva, E. G.; Gryczynski, I.; Terpetschnig, E. A.; Patsenker, L.; Laczko, G.; Borejdo, J.; Gryczynski, Z. Single Molecule Studies of Multiple-fluorophore Labeled Antibodies. Effect of Homo-FRET on the Number of Photons Available before Photobleaching. *Curr. Pharm. Biotechnol.* **2008**, *9*, 411–420.

(12) Duhamel, J. Global Analysis of Fluorescence Decays to Probe the Internal Dynamics of Fluorescently Labeled Macromolecules. *Langmuir* **2014**, *30*, 2307–24.

(13) Borodavka, A.; Tuma, R.; Stockley, P. G. A Two-stage Mechanism of Viral RNA Compaction Revealed by Single Molecule Fluorescence. *RNA Biol.* **2013**, *10*, 481–489.

(14) Usselman, R. J.; Walter, E. D.; Willits, D.; Douglas, T.; Young, M.; Singel, D. J. Monitoring Structural Transitions in Icosahedral Virus Protein Cages by Site-directed Spin labeling. *Journal Of The American Chemical Society* **2011**, *133*, 4156–4159.

(15) Kao, C. C.; Sivakumaran, K. Brome Mosaic Virus, Good for an RNA Virologist's Basic Needs. *Mol. Plant Pathol.* **2000**, *1*, 91–97.

(16) Lucas, R. W.; Larson, S. B.; McPherson, A. The Crystallographic Structure of Brome Mosaic Virus. *J. Mol. Biol.* **2002**, *317*, 95–108.

(17) Bancroft, J. B.; Hills, G. J.; Markham, R. A Study of the Self-assembly Process in a Small Spherical Virus. Formation of Organized Structures from Protein Subunits In Vitro. *Virology* **1967**, *31*, 354–379.

(18) Speir, J. a.; Munshi, S.; Wang, G.; Baker, T. S.; Johnson, J. E. Structures of the Native and Swollen Forms of Cowpea Chlorotic Mottle Virus Determined by X-ray Crystallography and Cryo-electron Microscopy. *Structure* **1995**, *3*, 63–78.

(19) Michael, T.; Wilson, A. Cotranslational Disassembly Increases the Efficiency of Expression of TMV RNA in Wheat Germ Cell-free Extracts. *Virology* **1984**, *356*, 353–356.

(20) Albert, F. G.; Fox, J. M.; Young, M. J. Virion Swelling is Not Required for Cotranslational Disassembly of Cowpea Chlorotic Mottle Virus in Vitro. *J. Virol.* **1997**, *71*, 4296–9.

(21) Förster, T. Zwischenmolekulare Energiewanderung und Fluoreszenz. *Ann. Phys.* **1948**, *437*, 55–75.

(22) Kloczkowski, A.; Kolinski, A. In *Theoretical Models and Simulations of Polymer Chains in Physical Properties of Polymers Handbook*; Mark, J. E., Ed.; Springer, 2007; pp 67–81.

(23) Jackson, J. D. *Wiley*; Wiley, 2007; p 832.

(24) Johnson, J. M.; Tang, J.; Nyame, Y.; Willits, D.; Young, M. J.; Zlotnick, A. Regulating Self-assembly of Spherical Oligomers. *Nano Lett.* **2005**, *5*, 765–70.

(25) Garmann, R. F.; Comas-Garcia, M.; Gopal, A.; Knobler, C. M.; Gelbart, W. M. The Assembly Pathway of an Icosahedral Single-stranded RNA Virus Depends on the Strength of Inter-subunit Attractions. *J. Mol. Biol.* **2014**, *426*, 1050–60.

(26) Gopal, A.; Zhou, Z. H.; Knobler, C. M.; Gelbart, W. M. Visualizing Large RNA Molecules in Solution. *RNA* **2012**, *18*, 284–99.

(27) Gopal, A.; Egecioglu, D. E.; Yoffe, A. M.; Ben-Shaul, A.; Rao, A. L. N.; Knobler, C. M.; Gelbart, W. M. Viral RNAs Are Unusually Compact. *PLoS One* **2014**, *9*, e105875.

Graphical TOC Entry

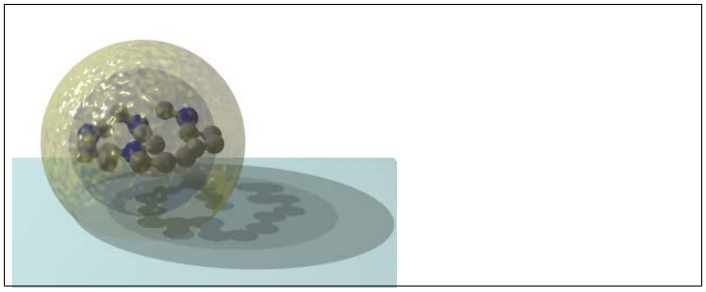

In singulo experimental measurement of multiply-labeled viral RNA dynamics